Presented at Emerging Lithographic Technologies VIII, *Proc. SPIE* **5374**, *pp* 64-73.

EUV interferometric testing and alignment of the 0.3 NA MET optic

Kenneth A. Goldberg*, Patrick Naulleau, Paul Denham, Senajith B. Rekawa,
Keith Jackson, J. Alexander Liddle, Erik H. Anderson
Center for X-Ray Optics, Lawrence Berkeley National Laboratory, Berkeley, CA 94720

ABSTRACT

Extreme ultraviolet (EUV) interferometry has been successfully performed for the first time at 0.3 numerical aperture (NA). Extensive EUV "at-wavelength" testing including alignment, was performed on a newly created Micro Exposure Tool (MET) optic designed for sub-50-nm EUV lithographic imaging experiments. The two-mirror, 0.3 NA MET is arguably the highest resolution light-projection lithography tool ever made. Using both lateral shearing and phase-shifting point-diffraction interferometry, the wavefront was measured across the field of view, and the alignment was optimized in preparation for imaging. The wavefront quality reached 0.55 nm RMS ($\lambda_{EUV}/24.5$) in a 37-term annular Zernike polynomial series, dominated by higher-order spherical aberration. Measurements included calibrations of the interferometer accuracy, assessment of repeatability, and cross-comparisons of visible and EUV interferometric measurements. The comparisons and the final, measured wavefront quality were affected by an apparent alignment drift, several tenths of a nm in magnitude. Significant unresolved differences between testing strategies shows that continued work is needed to improve the measurement accuracy to levels required for EUV lithography.

Keywords: extreme ultraviolet interferometry, extreme ultraviolet lithography, EUV, at-wavelength testing, MET.

1. INTRODUCTION

A new generation of 0.3 numerical aperture (NA) prototype extreme ultraviolet (EUV) optical systems is being produced to provide an opportunity for early learning with sub-50-nm EUV imaging. Developed for static micro-field imaging, these two-mirror, 0.3 NA, *Micro-Exposure Tool* (MET) optics operate at 13.5-nm wavelength, and have a design Rayleigh resolution of 27-nm.[1,2,3] They hold the promise of even higher resolutions achieved with tailored illumination conditions. Visible-light and EUV wavefront measurements of the MET reveal it to be one of the highest resolution light-projection lithography tools ever made.

In order to achieve optimal, diffraction-limited performance, EUV optical systems require alignment to sub-nanometer aberration tolerances. Wavefront aberrations of a few tenths of a nanometer can cause a significant reduction in the process window. While image-printing and certain aerial image monitoring configurations will provide some wavefront quality feedback, at these high resolutions, detailed quantitative system measurements are only available from interferometry. Ultra-high-accuracy interferometry is a cornerstone requirement for the success of these and future optics, and represents a strategic risk-reduction step for these expensive developmental optics. Operating at the design EUV wavelength, EUV interferometry has been used in the diagnosis and remediation several types of fabrication and system-alignment errors, in the assessment of chromatic effects and flare, and most importantly, in the optimization of imaging performance.[4,5,6,7]

In principle, if the mirror surfaces are clean and the multilayer profiles are well known, then predictable angle- and polarization-dependent phase differences can be accounted for, and the EUV and visible-light measurements will agree. However, for EUV optics, the required system wavefront accuracies approach or exceed the accuracy limits of the interferometers used to test them. Active collaborations between researchers at Lawrence Livermore National Laboratory (LLNL) and Lawrence Berkeley National Laboratory (LBNL), in the cooperative measurement of eight different prototype EUV optics, have improved our confidence in ultra-high accuracy interferometry in the 100-pm domain. Careful intercomparisons have led to the discovery and remediation of several systematic error sources that would have been

*KAGoldberg@lbl.gov; phone 1 510 495-2261; fax 1 510 486-4550; www-cxro.lbl.gov

difficult to diagnose in isolation. Such an opportunity was available in one of the MET optics, which was aligned and measured at LLNL before being brought to LBNL for continued alignment in preparation for imaging.

This MET optic has been subjected to extensive interferometric testing in preparation for imaging experiments at LBNL. The individual mirror elements (convex M1, and concave M2) were fabricated and single-element interferometry was performed by Carl Zeiss. Multilayer coating and system assembly were performed at LLNL, where the optical housing was designed and built. Visible-light single-element measurements were made of the M1 mirror and alignment was performed by LLNL using a lensless visible-light PSDI. At the conclusion of visible-light alignment, the system was transferred to the Advanced Light Source (ALS) at LBNL where an EUV interferometer[2] is installed on an undulator beamline. Before shipping, careful measurements were made of the conjugate point positions; coordinate transfer was facilitated by a metrology tower comprised of in-vacuum CCD cameras and capacitance micrometers.

EUV interferometry was used to optimize the system alignment for imaging, and characterize it at-wavelength. Several different EUV interferometry techniques have been under development at LBNL since 1993. To date, nine separate EUV lithographic lenses have been measured and aligned; yet the measurement of the MET with its high (annular) 0.3 NA (three times higher than previous systems), presented the most significant measurement challenges. Systematic errors in the interferometer arise from the testing geometry and the relative alignment of the optical components. These errors can be measured and compensated using null-testing techniques. However, the systematic error magnitudes and alignment sensitivities generally scale as powers of the NA, making calibration measurements at 0.3 NA many times more important and difficult than similar measurements at 0.1 NA.

We report the results of EUV interferometry in two different configurations: cross-grating lateral shearing interferometry, and phase-shifting point-diffraction interferometry. In addition to the alignment, system stability is discussed, and an intercomparison with visible-light interferometry is presented.

2. WAVEFRONT MEASUREMENTS

High-accuracy wavefront measurements facilitate system optimization for high-resolution imaging. Alignment of the MET is performed by the actuation of a six-arm mount on the M1 mirror, and by the repositioning of the conjugate points in three-dimensions. The arm motion is driven by Picomotors which are designed for long-term stability when not in use. The most sensitive wavefront aberrations to arm actuation are coma, astigmatism and spherical aberration, in that order. The actuation of any single arm introduces roughly equivalent amounts of coma with an RMS magnitude of approximately 3.0 nm per µm of actuation. The same amount of actuation introduces approximately 0.17 nm of astigmatism, and 0.07 nm of spherical aberration.

The optic is designed to have a wafer-side field of view of 600 × 200 µm, 3 × 1 mm on the reticle-side, within tilted conjugate planes. A 4° reticle-plane tilt allows light reflected from the reticle to enter the optic parallel to the central axis of this rotationally symmetric system. Respecting the tilted conjugate planes (4° reticle, and 0.8° wafer), measurements were performed across a three-dimensional volume field of view; up to 27 points were measured per data set. The aberrations vary within the field, and the most significant dependencies are (approximately): 0.08 nm astigmatism, and 0.06 nm spherical aberration per mm of lateral displacement; and 0.10 nm coma and 1.66 nm spherical aberration per mm of longitudinal displacement (RMS aberration magnitudes). The 4° reticle tilt introduces a reticle-side longitudinal position change of ±35 µm across the narrow direction of the field, which adds ±36 pm RMS of spherical aberration.

The annular pupil shape, including the four narrow "spider" obstructions, requires the use of a basis set of aberration polynomials that is orthogonal on the measurement domain. Derived from the Zernike circle polynomials, these aberration terms form a proper basis for the alignment and characterization of the optical system. The quoted aberration coefficients always refer to such bases, although slightly different basis sets are used for different measurements and comparisons where more or less of the pupil domain is included. For annular pupils in general, differences between coefficients of the orthogonal basis and the conventional Zernike circle polynomials can be significant, especially for the spherical aberration terms.

Wavefront measurements were performed at a controlled temperature of 20.0°C, in a vacuum environment with a base pressure of 1×10^{-7} Torr. A partial pressure of oxygen gas at 4×10^{-5} Torr was introduced as a preventive measure, to mitigate carbon contamination of the pinholes. More information about the experimental system is available [Ref. 2].

2.1 Predicted system wavefront

Prior to assembly, the individual mirror elements were measured by Carl Zeiss, and separately, the convex M1 mirror was measured by LLNL. Based on the initial individual mirror wavefronts, the system wavefront at the central field point was predicted to have an RMS wavefront aberration magnitude of 0.17 nm in the first 37 Zernike terms. However the LLNL measurement of M1 showed the presence of a higher-order spherical aberration with an aberration magnitude of 0.22 nm, which in reflection could contribute 0.44 nm to the total system wavefront.[8]

2.2 Visible-light measurement

At the conclusion of visible-light alignment, the total system wavefront error was 0.56 nm RMS in a 37-term annular Zernike series, dominated by 0.49 nm of higher-ordered spherical aberration; close to the value predicted by the LLNL M1 single-element testing. The astigmatism, coma, and spherical aberration were reduced to 0.15, 0.10, and 0.05 nm respectively.[8] The visible-light measurements cover a limited radial sub-domain of the full pupil: 10–26 mm radius out of a full pupil radius of 8.4–27 mm, or 87% of the full area. Reductions of the measurement domain can lead to an underestimation of the full pupil's wavefront aberration magnitude; thus comparisons are performed on identical domains.

2.3 EUV interferometry methods

Prior to quantitative tests at wavelength, the first inspection was performed using the well-known Foucault, or *knife-edge* test: half the beam is blocked at focus by a sharp edge. In the direction perpendicular to the edge, changes in the wavefront slope are projected as variations in the intensity, as shown in Fig. 1. These two measurements unambiguously indicate the presence of higher-order spherical aberration.

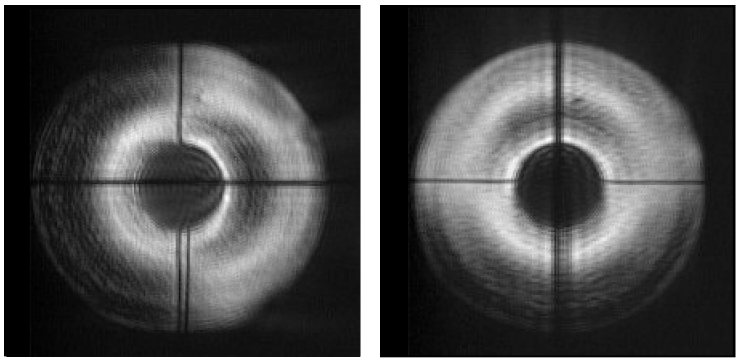

Fig. 1. Foucault or "knife-edge" test. The Foucault test converts wavefront slope variations in into intensity variations, in one direction at a time. These measurements (vertical edge on the left, horizontal edge on the right) unambiguously indicate the presence of a higher-order spherical aberration.

Two very different, quantitative EUV wavefront measurement methods were used to measure the MET: lateral shearing interferometry (LSI), using a cross-grating configuration,[2,9] and phase-shifting point-diffraction interferometry (PS/PDI).[2,10] There are specific advantages and disadvantages to each technique.

2.3.1 Lateral shearing interferometer. Owing to its ease of alignment and tolerance for larger errors, the LSI was the primary measurement method. A two dimensional "cross" grating is placed in the first Talbot plane beyond the focal plane. Several different gratings were available on an image-plane mask; our most common configuration was a 1.5-µm-pitch grating placed 76.9 µm beyond the focal plane, producing approximately 32 fringes across the pupil. Shearing is a self-referential technique that relies on the interference of the test beam with displaced copies of itself. As such, regions adjacent to any pupil boundary must be excluded, and the measurement area is reduced by approximately 3%. The interference pattern can be analyzed to produce approximations to the wavefront gradient in two directions simultaneously. Reconstruction of the original test wavefront is performed using zonal[11] and modal[12,13] techniques, and both reconstruction methods were employed during the measurements. We are still evaluating the advantages and error sensitivities of these methods; typically the discrepancies were on the order of 0.05 nm or smaller for individual aberration coefficients.

2.3.2 Phase-shifting point-diffraction interferometer. Using diffraction from a pinhole in the image plane, the PS/PDI offers direct wavefront measurement through comparison of the test beam with a highly spherical reference wavefront. We regard the PS/PDI as the accuracy standard for our EUV wavefront measurements. However, relevant pinhole sizes for PS/PDI testing at 0.3 NA are between 20 and 35 nm.[2,3] With Ni as the absorber material of choice, mask opacity requirements necessitate the use of 150–200-nm-thick films, making pinhole fabrication a significant challenge. Furthermore, the alignment of the interferometer requires 10–15 nm lateral pinhole positioning, 100 nm longitudinally. This small capture range is reduced in the presence of wavefront aberrations whose magnitude decreases the Strehl ratio and lowers the available peak intensity at focus.

PS/PDI pinhole masks were fabricated using the Nanowriter, an electron-beam lithography tool at the Center for X-Ray Optics (CXRO), LBNL. The potentially-low transmission efficiency of small pinholes raises the opacity requirements of the mask, necessitating the use of a thicker absorber layer, and compounding the difficulties of pinhole fabrication. Pinholes used in the experiment were fabricated in 140-nm-thick, free-standing Ni membranes.[2,3]

2.4 EUV wavefront measurements

Over the course of several months, thousands of individual wavefront measurements were made. Using LSI, the wavefront was measured across the field of view eleven separate times. The most significant of those measurements are: (1) the first measurement at 20.0°C, which enables comparison with the final visible-light measurement; (2) the optimized alignment, which shows the highest achieved wavefront quality; and (3) the final alignment state of the optic, measured one month after the final alignment procedure.

When LSI was used to measure the wavefront across the field of view, measurements were made at nine or more separate points, covering the corners, edges, and center of the field within the tilted conjugate planes. Three wavefront measurement sets are shown in Figs. 2, 7, and 8. Within each of these figures, the individual wavefronts are shown on a grayscale spanning the range [–1, 1 nm]. (Piston, tilt, and defocus terms are removed from the analysis.) The diameter of each wavefront shown is proportional to the 37-term RMS wavefront error magnitude (smaller is better). The most significant wavefront aberration terms, and those involved in the system alignment, are shown to the right of each figure. In the figures, spherical aberration is written as "sph ab"; higher-order spherical aberration, a combination of four rotationally symmetric terms beyond defocus and primary spherical aberration is written as "h-o sph".

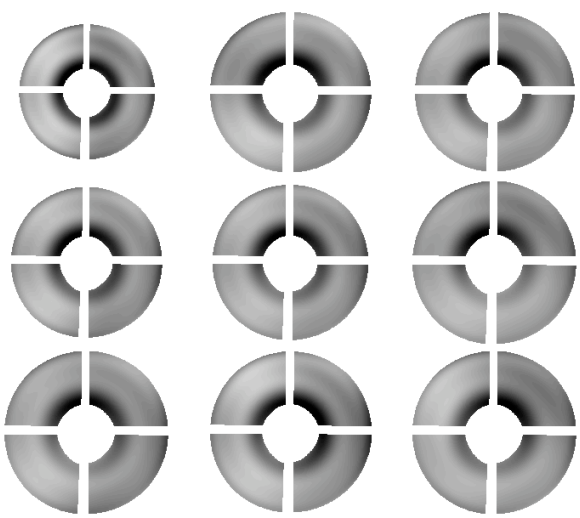

[nm] RMS

σ37 = 1.04	σ37 = 1.23	σ37 = 1.22
astig = 0.05	astig = 0.47	astig = 0.11
coma = 0.24	coma = 0.55	coma = 0.56
sph ab = 0.82	sph ab = 0.82	sph ab = 0.86
trifoil = 0.12	trifoil = 0.19	trifoil = 0.16
h-o sph = 0.37	h-o sph = 0.36	h-o sph = 0.38
σ37 = 1.15	σ37 = 1.19	σ37 = 1.32
astig = 0.24	astig = 0.29	astig = 0.21
coma = 0.32	coma = 0.45	coma = 0.70
sph ab = 0.89	sph ab = 0.86	sph ab = 0.85
trifoil = 0.13	trifoil = 0.09	trifoil = 0.12
h-o sph = 0.37	h-o sph = 0.38	h-o sph = 0.37
σ37 = 1.27	σ37 = 1.23	σ37 = 1.31
astig = 0.29	astig = 0.43	astig = 0.42
coma = 0.60	coma = 0.34	coma = 0.50
sph ab = 0.84	sph ab = 0.94	sph ab = 0.96
trifoil = 0.12	trifoil = 0.10	trifoil = 0.05
h-o sph = 0.37	h-o sph = 0.38	h-o sph = 0.37

Fig 2. July 2, 2003: Wavefront measurements at nine points spanning the field of view. The grayscale range is [–1,1]. As shown, the diameters of the wavefronts are proportional to the 37-term RMS wavefront error magnitudes of each, labeled σ37.

2.4.1 First EUV LSI measurement, and PSDI comparison. Figure 2 shows the first EUV field measurement at 20°C. The wavefront contains a large, unexpected, primary spherical aberration component (0.80 nm RMS). A comparison between this first EUV measurement and the final visible-light measurement is shown in Figs. 3 and 4, and in Table 1. (Relative to the position used as the center of the EUV field, the visible-light measurement was made at a position displaced along the $+x$ axis. Interpolation of the aberration coefficients is used to predict the EUV wavefront at the corresponding point.) The significant measurement differences are on the order of 1 nm—as large as the wavefront error itself. With this limited data, the differences cannot be specifically attributed to differences between the two interferometers or changes in the system alignment that may have occurred during shipping and installation—both are possible explanations. In fact, abrupt changes in the spherical aberration magnitude were observed on several occasions. While primary spherical aberration is the most significant difference, other differences appear, including terms that are not related to the alignment, such as trifoil. When the spherical aberration is subtracted from the comparison, the RMS difference is 0.79 nm, as shown in Fig. 4b. Both measurements show similar contributions from the higher-order spherical aberration terms, with a EUV magnitude of 0.35 nm and a visible-light magnitude of 0.41 nm RMS.

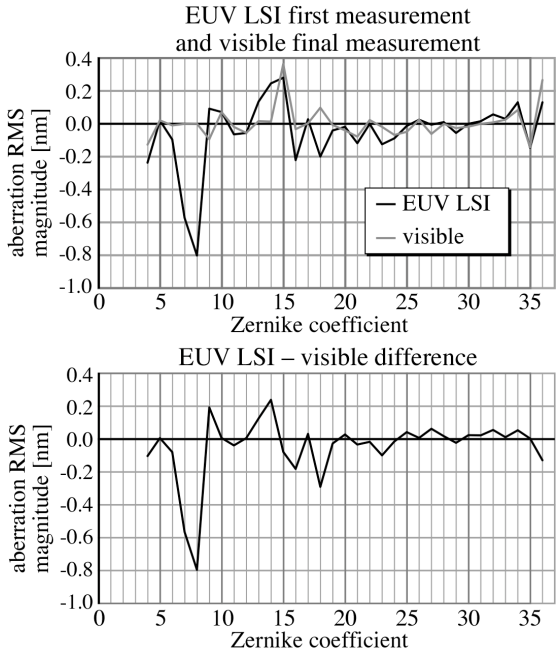

Table 1. EUV LSI and visible-light PSDI aberration polynomial coefficients.

j	EUV LSI	visible PSDI	diff.	
4	-0.24	-0.13	-0.11	astig.
5	0.02	0.02	0.00	
6	-0.10	-0.01	-0.09	coma
7	-0.57	0.00	-0.57	
8	-0.80	0.00	-0.80	sph. ab.
9	0.09	-0.09	0.19	trifoil
10	0.07	0.07	0.00	
11	-0.06	-0.02	-0.05	2nd astig.
12	-0.06	-0.06	0.00	
13	0.14	0.02	0.12	2nd coma
14	0.25	0.01	0.23	
15	0.28	0.37	-0.08	2nd sph. ab.
16	-0.22	-0.03	-0.19	4θ
17	0.03	0.00	0.02	
18	-0.20	0.10	-0.30	2nd trifoil
19	-0.04	-0.01	-0.03	
σ37	**1.19**	**0.55**	**1.13**	
PV	6.47	3.31	6.53	

Fig. 3. Aberration polynomial coefficients measured on a pupil subdomain common to both LSI and PSDI. The upper plot shows the EUV LSI (black) and visible PSDI (gray) coefficients together. The lower plot is the subtractive difference of the two.

(a) Full comparison

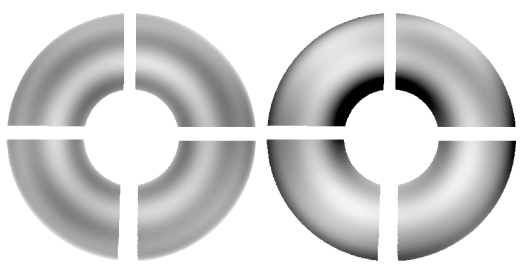

	visible	EUV LSI	difference
σ_{37}	0.55	1.19	1.13
PV	3.31	6.47	6.53

(b) Comparison with spherical aberration removed

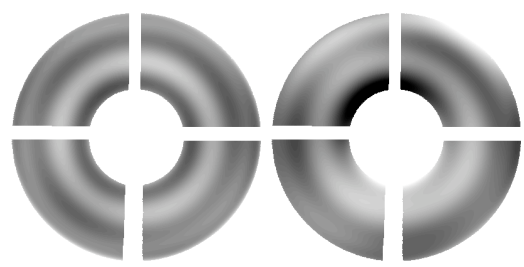

	visible	EUV LSI	difference
σ_{37}	0.55	0.87	0.79
PV	3.31	5.64	4.78

Fig. 4. First comparison of visible PSDI and EUV LSI wavefront measurements: wavefront phasemaps and statistics. **(a)** The full comparison; grayscale range [–3, 2 nm]. **(b)** Comparison with spherical aberration (the primary difference) removed; grayscale range: [–2.4, 2.4 nm].

2.4.2 First EUV alignment, and EUV PS/PDI comparison. The system alignment was optimized using LSI as preparations were made to re-configure the system for imaging. During the alignment iterations that were performed to optimize the MET wavefront across the field of view, the alignment stability became an issue of concern at the level of 0.1–0.2 nm RMS, in the astigmatism, coma, and spherical aberration terms. Short term changes, mainly in coma and astigmatism, were observed in the minutes following alignment steps. More abrupt, unpredictable coma and spherical aberration changes were also detected in the hours following alignment; often these were 0.2–0.3 nm RMS in magnitude. For the latter cases, it appeared that the change would occur once and that the system would be stable afterward. In one case, a vent/pump cycle following alignment appears to have triggered a change in the alignment state despite the fact that the venting (to nitrogen) occurs in a very slow, controlled manner.

Following the first system EUV alignment, the interferometer was changed into the PS/PDI configuration, requiring a vent. The PS/PDI measurements, performed during the next two days, showed a primary spherical aberration not present in the LSI measurements: a change of 0.36 nm (see Fig. 5 and 6a). After a thorough re-evaluation of the separate data

analysis methods used in the LSI and the PS/PDI, we concluded that the observed measurements differences are likely not coming from differences in the analysis. We believe that the changes come from a discreet change in the system alignment state.

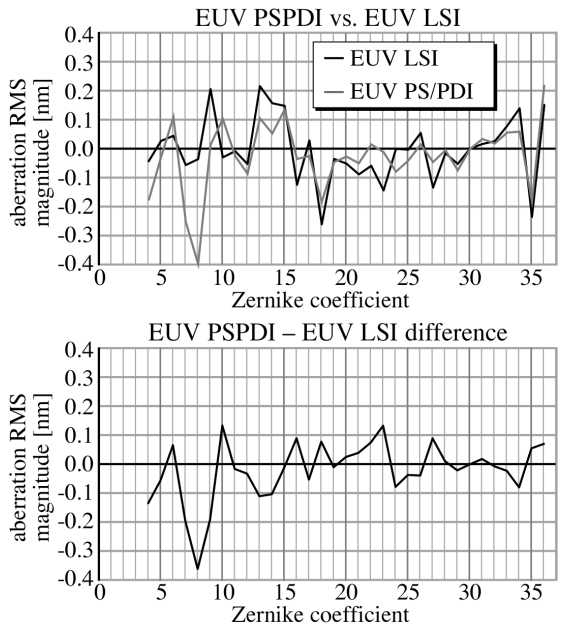

Table 2. EUV PS/PDI and LSI aberration polynomial coefficients.

j	EUV PS/PDI	EUV LSI	diff.	
4	−0.18	−0.04	−0.14	astig.
5	−0.03	0.03	−0.06	
6	0.11	0.04	0.06	coma
7	−0.25	−0.06	−0.20	
8	−0.40	−0.04	−0.36	sph. ab.
9	0.01	0.21	−0.19	trifoil
10	0.10	−0.03	0.13	
11	−0.03	−0.01	−0.02	2nd astig.
12	−0.09	−0.05	−0.03	
13	0.10	0.22	−0.11	2nd coma
14	0.05	0.16	−0.10	
15	0.13	0.15	−0.01	2nd sph. ab.
16	−0.04	−0.12	0.09	4θ
17	−0.03	0.03	−0.05	
18	−0.18	−0.26	0.08	2nd trifoil
19	−0.05	−0.04	−0.01	
σ37	**0.65**	**0.63**	**0.57**	
PV	3.05	4.45	3.82	

Fig. 5. Aberration polynomial coefficients measured on a pupil subdomain common to both LSI and PS/PDI. The upper plot shows the LSI (black) and PS/PDI (gray) coefficients together. The lower plot is the subtractive difference of the two.

(a) Full comparison

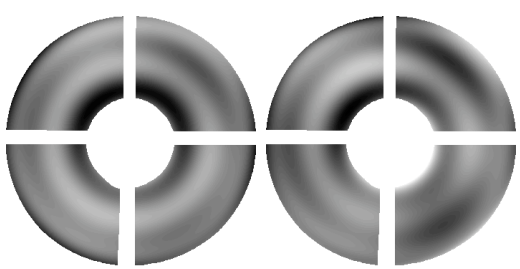

	PS/PDI	EUV LSI	difference
σ_{37}	0.65	0.63	0.57
PV	3.05	4.45	3.82

(b) Comparison with spherical aberration removed

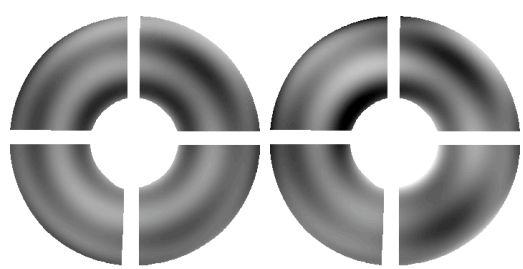

	PS/PDI	EUV LSI	difference
σ_{37}	0.53	0.63	0.46
PV	2.89	4.47	3.59

Fig. 6. Comparison of EUV PS/PDI and EUV LSI wavefront measurements: wavefront phasemaps and statistics. **(a)** The full comparison; grayscale range [–1.9, 2.6 nm]. **(b)** Comparison with spherical aberration (the primary difference) removed; grayscale range [–1.7, 2.7 nm].

2.4.3 Final alignment and stability measurements. Before the transition to imaging configuration, the system alignment was optimized for the last time on September 25, 2003. The LSI field measurement is shown in Fig. 7. The 37-term RMS wavefront error magnitude reached an optimized value of 0.55 nm ($\lambda_{EUV}/24.5$) at the central field point.

The wavefront was measured several more times as the system sat virtually undisturbed for approximately one month. At one point during that period the temperature control system was accidentally deactivated for 12 hours causing the chamber temperature to rise by 1°C. We observed temperature-dependent changes in the wavefront as the system recovered its stable, 20.0°C temperature set point. Even at the constant temperature, the wavefront aberrations, coma in particular, drifted away from the optimized state. The final field measurement is shown in Fig. 8. The 37-term RMS wavefront error magnitude at the central field point was 0.80 nm ($\lambda_{EUV}/16.9$). In the imaging configuration, we retain the ability to translate the field of view so that we may cover the region of the highest wavefront quality, if it has shifted.

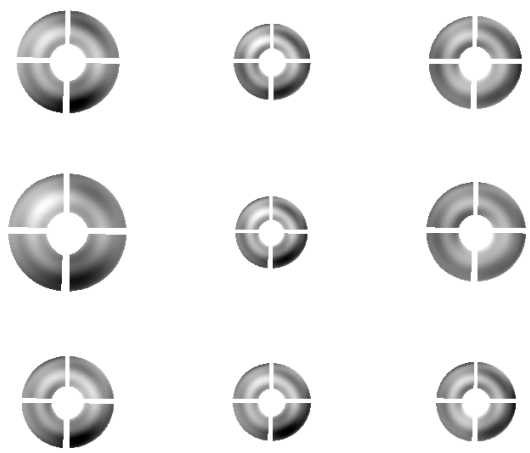

[nm] RMS

σ37 = 0.79	σ37 = 0.59	σ37 = 0.71
astig = 0.56	astig = 0.12	astig = 0.26
coma = 0.10	coma = 0.12	coma = 0.24
sph ab = 0.07	sph ab = 0.05	sph ab = 0.04
trifoil = 0.13	trifoil = 0.13	trifoil = 0.12
h-o sph = 0.37	h-o sph = 0.36	h-o sph = 0.37
σ37 = 0.90	σ37 = 0.55	σ37 = 0.76
astig = 0.59	astig = 0.04	astig = 0.19
coma = 0.37	coma = 0.06	coma = 0.36
sph ab = 0.01	sph ab = 0.04	sph ab = 0.02
trifoil = 0.19	trifoil = 0.14	trifoil = 0.12
h-o sph = 0.38	h-o sph = 0.37	h-o sph = 0.36
σ37 = 0.71	σ37 = 0.60	σ37 = 0.61
astig = 0.38	astig = 0.25	astig = 0.13
coma = 0.23	coma = 0.11	coma = 0.14
sph ab = 0.01	sph ab = 0.02	sph ab = 0.01
trifoil = 0.12	trifoil = 0.12	trifoil = 0.11
h-o sph = 0.37	h-o sph = 0.36	h-o sph = 0.36

Fig 7. September 25, 2003: Optimized alignment.

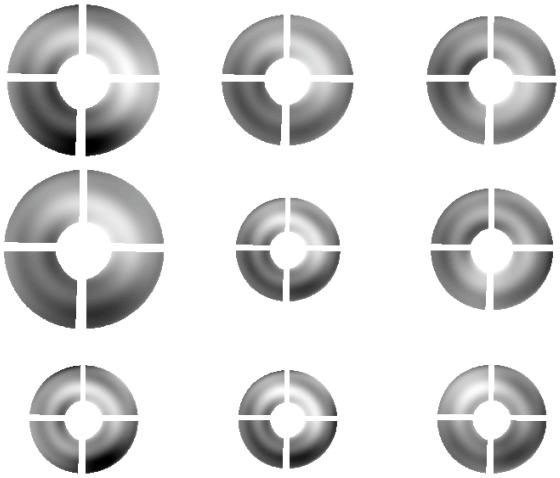

[nm] RMS

σ37 = 1.16	σ37 = 1.00	σ37 = 0.99
astig = 0.72	astig = 0.07	astig = 0.28
coma = 0.73	coma = 0.80	coma = 0.69
sph ab = 0.02	sph ab = 0.16	sph ab = 0.06
trifoil = 0.26	trifoil = 0.09	trifoil = 0.12
h-o sph = 0.36	h-o sph = 0.36	h-o sph = 0.36
σ37 = 1.22	σ37 = 0.80	σ37 = 0.94
astig = 0.41	astig = 0.07	astig = 0.39
coma = 0.96	coma = 0.56	coma = 0.52
sph ab = 0.01	sph ab = 0.08	sph ab = 0.04
trifoil = 0.18	trifoil = 0.15	trifoil = 0.11
h-o sph = 0.38	h-o sph = 0.36	h-o sph = 0.37
σ37 = 0.83	σ37 = 0.76	σ37 = 0.83
astig = 0.48	astig = 0.03	astig = 0.30
coma = 0.34	coma = 0.51	coma = 0.49
sph ab = 0.03	sph ab = 0.04	sph ab = 0.03
trifoil = 0.15	trifoil = 0.08	trifoil = 0.23
h-o sph = 0.37	h-o sph = 0.37	h-o sph = 0.37

Fig 8. October 24, 2003: Final field measurement.

2.4.4 Three-way comparison. Despite the alignment issues that cause uncertainties in the astigmatism, coma, and spherical aberration, a three-way comparison can be performed among the remaining aberration terms (Fig. 9). While the main purpose of the alignment is to minimize these three aberration terms, and removing them from consideration does eliminate the most important elements of the comparison, such a study reveals other differences between the measurements beyond the low-spatial-frequency alignment modes. In particular, the similarity in the higher-ordered spherical aberration measurement is evident; and between the two EUV measurements, very similar wavefront shapes are apparent. Yet there are clear differences between the visible-light and EUV measurements in the non-rotationally symmetric terms; and between the two EUV measurements, it appears that the LSI overestimates the aberration magnitudes by approximately 0.1 nm in this case.

2.4.5 Measurement precision. Repeated measurement of the system wavefront creates a large body of data that can be studied to determine the stability and repeatability of the interferometry itself. Such analysis is especially important in the presence of a suspected system alignment instability: to what extent can we be sure that we are not seeing differences brought on by the interferometry itself?

(a) Full spatial frequency content of the measurements.

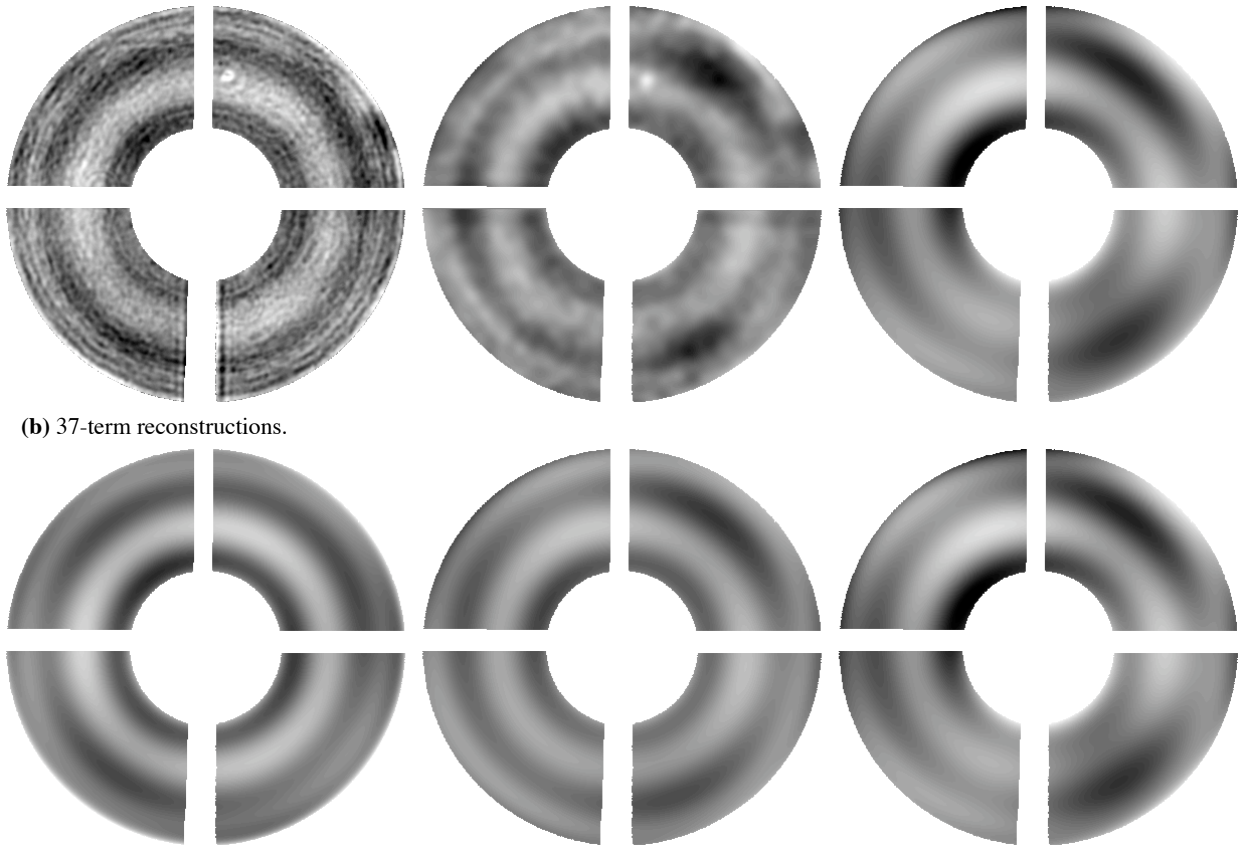

(b) 37-term reconstructions.

visible-light PSDI base	EUV PS/PDI base	EUV LSI (shearing) base
σ_{37} = 0.39 nm	σ_{37} = 0.31 nm	σ_{37} = 0.44 nm
PV =3.15 nm	PV = 2.11 nm	PV = 3.57 nm

Fig. 9. Three-way comparison with astigmatism, coma, and spherical aberration *removed* from consideration. **(a)** The phasemaps contain the full spatial-frequency content of the original measurements, which is different for each interferometer. **(b)** 37-term reconstructions on which the wavefront statistics are based. Grayscale ranges are [–1.7, 2.0 nm].

There are three primary ways to assess the repeatability of the LSI interferometry. The first is to calculate the *instantaneous repeatability* of the measurements; that is, when a series of sequential measurements are made, how self-consistent are the results? This measurement sets the upper limit of the repeatability that can be expected from other tests that take place over longer time spans. Analysis of hundreds of measurement sets consisting of 4-6 interferograms each, shows that the standard deviation of the individual aberration coefficients is 17 pm for spherical aberration, 112 pm for coma, 54 pm for secondary coma, and 59 pm for astigmatism. All other terms are below 32 pm, most are below 20 pm.

A second test of the measurement repeatability is the self-consistency of measurements made across the field. In these tests, different object pinholes and different regions of the grating beamsplitter are used. Furthermore, the entire optical system is translated by 3 mm during the measurements, which can take 2-4 hours to perform. Data presented in Figs. 2, 7, and 8 show that point-to-point variations are limited to a few hundred pm at most, and significantly smaller for most terms. Most of the relative, point-to-point variation is consistent with the other field measurements, arising from the natural aberration field dependence of the MET. Therefore, the combined effect of changing many measurement parameters is not larger than the differences we are attributing to alignment instability.

A third test of the measurement precision comes from the alignment process itself. As the system is aligned, step-by-step, measurements are made before and after every adjustment. Taking into account the uncertainties that accompany Picomotor-actuated adjustments on the scale from 30 nm to 2 µm, the results of arbitrary alignments were predictable to 100 pm, and often to better than 50 pm. This shows that the precision of the interferometric measurements is on par with or is better than those values.

3. CONCLUSION

The measurements presented here demonstrate the successful application of at-wavelength interferometry to an EUV optical system with 0.3 NA. Using both LSI and PS/PDI, repeated measurements were made across the field of view during alignment optimization, in preparation for imaging. Interferometry and alignment brought the system to a diffraction-limited RMS wavefront error quality of 0.55 nm ($\lambda_{EUV}/24.5$) in a 37-term series. The wavefront error is dominated by a higher-order spherical aberration term that was predicted by visible-light measurements of the isolated M1 mirror and of the assembled system.

These measurements provide a rare and important opportunity for cross-comparison between visible-light and two EUV interferometry techniques. However, an apparent alignment drift complicated the alignment and the comparisons considerably. With the system at rest, only small, slow wavefront changes were observed over a period of days. However, measurements made before and after transportation from LLNL to LBNL, and also on several occasions at LBNL when the configuration of the interferometer was changed in a way that required a vent/pump cycle, show significant changes in spherical aberration and coma. Unknown changes to the alignment state thus compromise our ability to compare different wavefront measurement methods. Nonetheless, the visible-EUV comparison reached an agreement of approximately 1 nm, with good similarity in the higher-order spherical aberration measurement, but little agreement in the lowest-spatial-frequency terms, those associated with the system alignment. The EUV LSI–PS/PDI comparison showed agreement at the level of 0.57 nm RMS, or 0.46 nm when the primary difference, spherical aberration, was removed. These difference magnitudes represent a large fraction of the total wavefront error, leading us to the conclusion that the overall accuracy is thus far limited to approximately 0.5 nm. Improved shearing data analysis methods may improve the level of agreement between the two EUV techniques, and are the subject of ongoing research.

Following the final system alignment, the wavefront error magnitude at the central field point drifted upward slowly, reaching 0.80 nm ($\lambda_{EUV}/17$) after one month, yet maintaining "diffraction-limited" quality.

ACKNOWLEDGMENTS

This work would not have been possible without the hard work of the CXRO members, including Brian Hoef, Kevin Bradley, M. Gideon Jones, Ron Oort, Drew Kemp, Farhad Salmassi, René Delano, Al Rawlings, Ron Tackaberry, Robert Gunion, Hanjing Huang, Jeff Gamsby, Bruce Harteneck, and David Attwood. Additional thanks are due for the contributions of LLNL researchers including, John Taylor, Don Phillion, Layton Hale, Mike Johnson, Henry Chapman, Nhan Nguyen, Carl Chung, and Gary Sommargren. The authors are also indebted to Kim Dean of International Sematech and Pat Gabella of AMD for their support and guidance. This work is funded by the International Sematech, and by the U.S. Department of Energy.

REFERENCES

1. R. Hudyma, J. Taylor, D. Sweeney, L. Hale, W. Sweatt, N. Wester, "E-D characteristics and aberration sensitivity of the Microexposure tool (MET)," 2nd International EUVL Workshop, October 19–20, 2000 (http://www.sematech.org/public/resources/litho/meetings/euvl/20001019/hudyma.pdf)
2. K. A. Goldberg, P. Naulleau, P. Denham, S. B. Rekawa, K. Jackson, E. H. Anderson, J. A. Liddle, J. Bokor, "EUV Interferometry of the 0.3 NA MET Optic," *Proc. SPIE* **5037**, 69–74 (2003).
3. K. A. Goldberg, P. Naulleau, P. Denham, S. B. Rekawa, K. Jackson, E. H. Anderson, J. A. Liddle, J. Bokor, "Preparations for at-wavelength interferometry of the 0.3 NA Micro Exposure Tool optic," *J. Vac. Sci. & Technol. B***21** (6), 2706–10 (2003).
4. K. A. Goldberg, P. Naulleau, J. Bokor, and H. N. Chapman, "Honing the accuracy of extreme ultraviolet optical system testing: at-wavelength and visible-light measurements of the ETS Set-2 projection optic," *Proc. SPIE* **4688**, 329–337 (2002).
5. P. Naulleau, K. A. Goldberg, E. H. Anderson, P. Batson, P. E. Denham, K. H. Jackson, E. M. Gullikson, S. Rekawa, and J. Bokor, "At-wavelength characterization of the extreme ultraviolet Engineering Test Stand Set-2 optic," *J. Vac. Sci. & Technol. B***19** (6), 2396–2400 (2001).

6. P. Naulleau, K. Goldberg, E. Gullikson, and J. Bokor, "At-wavelength, system-level flare characterization of EUV optical systems," *Appl. Opt.* **39** (17), 2941–47 (2000).
7. J. E. M. Goldsmith, K. W. Berger, D. R. Bozman, G. F. Cardinale, D. R. Folk, C. C. Henderson, D. J. O'Connell, A. K. Ray-Chaudhuri, K. D. Stewart, D. A. Tichenor, H. N. Chapman, R. J. Gaughan, R. M. Hudyma, C. Montcalm, E. A. Spiller, J. S. Taylor, J. D. Williams, K. A. Goldberg, E. M. Gullikson, P. Naulleau, J. L. Cobb, "Sub-100-nm lithographic imaging with the EUV 10x Microstepper," *Proc. SPIE* **3676**, 264–71 (1999).
8. K. A. Goldberg, P. Naulleau, P. Denham, S. B. Rekawa, K. Jackson, E. H. Anderson, J. A. Liddle, J. Bokor, "Preparations for at-wavelength interferometry of the 0.3 NA Micro Exposure Tool optic," *J. Vac. Sci. & Technol. B* **21** (6), 2706–10 (2003).
9. P. P. Naulleau, K. A. Goldberg and J. Bokor, "Extreme ultraviolet carrier-frequency shearing Interferometry of a lithographic four-mirror optical system," *J. Vac. Sci. & Technol. B***18** (6), 2939–43 (2000).
10. P. P. Naulleau, K. A. Goldberg, S. H. Lee, C. Chang, D. Attwood, and J. Bokor, "Extreme-ultraviolet phase-shifting point-diffraction interferometer: a wave-front metrology tool with subangstrom reference-wave accuracy," *Appl. Opt.* **38** (35), 7252–63 (1999).
11. M. P. Rimmer, "Method for evaluating lateral shearing interferograms," *Appl. Opt.* **13** (3), 623–29 (1974).
12. G. Harbers, P. J. Kunst, and G. W. R. Leibbrandt, "Analysis of lateral shearing interferograms by use of Zernike Polynomials," *Appl. Opt.* **35** (31), 6162–72, 1996.
13. H. van Brug, "Zernike polynomials as a basis for wave-front fitting in lateral shearing interferometry," *Appl. Opt.,* **36** (13), 2788–90 (1997).